Journal of Alloys and Compounds 793 (2019) 56–64

Contents lists available at ScienceDirect

Journal of Alloys and Compounds

journal homepage: http://www.elsevier.com/locate/jalcom

Barium-induced effects on structure and properties of β-$Ca_3(PO_4)_2$-type $Ca_9Bi(VO_4)_7$

Nikolai G. Dorbakov [a], Vladimir V. Titkov [a], Sergey Y. Stefanovich [a], Oksana V. Baryshnikova [a], Vladimir A. Morozov [a], Alexei A. Belik [b], Bogdan I. Lazoryak [a, *]

[a] Chemistry Department, Moscow State University, 119991, Moscow, Russia
[b] Research Center for Functional Materials, National Institute for Materials Science, Namiki 1-1, Tsukuba, Ibaraki, 305-0044, Japan

ARTICLE INFO

Article history:
Received 26 November 2018
Received in revised form
11 March 2019
Accepted 26 March 2019
Available online 1 April 2019

Keywords:
Vanadates
Ferroelectric properties
Nonlinear optical properties
Crystal structure

ABSTRACT

$Ca_{9-x}Ba_xBi(VO_4)_7$ ($0 \le x \le 1.5$) solid solutions with the β-$Ca_3(PO_4)_2$-type structure were prepared by a solid-state method. Powder X-ray diffraction study of $0 \le x \le 0.7$ showed that Bi^{3+} and Ba^{2+} cations were completely incorporated into the β-TCP-type host framework up to $x = 0.7$. $Ca_{9-x}Ba_xBi(VO_4)_7$ ($x = 0.25$, 0.5) structures were refined by the Rietveld method using powder synchrotron X-ray diffraction data. DSC, SHG and dielectric properties measurements of $Ca_{9-x}Ba_xBi(VO_4)$ ($x = 0$, 0.25, 0.5) revealed two reversible first-order phase transitions (PT_1 and PT_2). Increase of Ba^{2+} content in $Ca_{9-x}Ba_xBi(VO_4)_7$ leads to lowering PT_1 and PT_2 phase transitions temperatures due to the increase of cell volume and the structure looseness. Nonlinear optical activity of $Ca_{9-x}Ba_xBi(VO_4)_7$ reaches its maximum response at $x = 0.5$. The amount of ($M1$–($M3$)–$M2$) dipoles in $Ca_{9-x}Ba_xBi(VO_4)_7$ ($0 < x \le 0.7$) structures increases with increasing Ba^{2+} content from 0.25 to 0.5 and decreases with changing x from 0.5 to 0.7.

1. Introduction

β-$Ca_3(PO_4)_2$ (β-TCP) [1] and $Ca_3(VO_4)_2$ [2] compounds with non-centrosymmetric structure (SG *R*3*c*, $Z = 21$) belong to the family of mineral whitlockite-related materials [3]. Size variations of the CaO_n polyhedra in the whitlockite-related structure allow to vary isovalent and aliovalent substitutions for Ca^{2+} cations and to obtain advanced materials with ferroelectric [4–6] and antiferroelectric [7], piezoelectric [8], nonlinear optical [5,9–12], ionic-conductive [4,5,13–16], luminescence [17–20] and non-linear laser [21,22] properties. These properties depend on chemical nature of cations, their number, and distribution in positions of crystal structure. The cation substitutions in the whitlockite-type framework allow obtaining multi-functional materials with the combination of properties such as high nonlinear optical activity, ferroelectricity, large ionic conductivity and high luminescence intensity.

The crystal chemical analysis [23] has shown that the whitlockite-type structure is suitable for isovalent and aliovalent substitutions of Ca^{2+} cations. Six cationic ($M1$-$M6$) positions present in the whitlockite-related structure. $M1$-$M3$ (18-*fold*) and $M5$ (6-*fold*) positions are always occupied while the occupation of $M4$ (6-*fold*) position can change from 0 to 1 and $M6$ (6-*fold*) position is usually vacant. Depending on the ionic radius, replacing cations substitute Ca^{2+} in different positions. An overview of cation distributions among the $M1$–$M5$ sites of the β-TCP-type structure is given in *Ref.* [24]. The presence of highly polarizable asymmetric metal-oxygen bonds and cations with a lone pair of electrons (Tl^+, Pb^{2+}, Bi^{3+}, Te^{4+}, I^{5+}) makes to increase the nonlinear optical activity of materials [25–29]. That is why the introduction of such cations into the whitlockite related structure is a promising way for obtaining materials with high optical nonlinearity.

This work studies ferroelectric and non-linear optical properties of $Ca_{9-x}Ba_xBi(VO_4)_7$ solid solutions and influence of cation distribution on their properties.

2. Experimental procedures

2.1. Materials and sample preparation

Powder samples of $Ca_{9-x}Ba_xBi(VO_4)_7$ were synthesized in the interval of $0 \le x \le 1.5$ in air by heating stoichiometric amounts of $CaCO_3$ (99.99%), Bi_2O_3 (99.8%), $BaCO_3$ (99.8%) and NH_4VO_3 (99.8%). Firstly, the stoichiometric mixture was heated up to 623 K for 7 h and kept at this temperature for 10 h. The obtained powder was

* Corresponding author.
E-mail address: bilazoryak@gmail.com (B.I. Lazoryak).

https://doi.org/10.1016/j.jallcom.2019.03.365
0925-8388/

mixed again and then heated up to 973 K for 10 h in air. The final synthesis was performed at 1173 K for 50 h with intermediate grindings and slow cooling in the furnace from 1173 K to room temperature (T_R) every 15–20 h.

2.2. Characterization

The element content was determined for the selected samples by inductively coupled plasma atomic emission spectroscopy with Agilent ICP-OES 5100 equipment. Substances were previously dissolved in hydrochloric acid (37%, Panreac, ISO grade). Signal detection was carried out at several wave-lengths for each element, the obtained values were averaged.

Differential scanning calorimetry (DSC) was carried out in Pt crucibles using a thermal analyzer SDT Q600 V8.1 Build 99 (TA Instruments) in air. The temperature range was 873–1173 K at the heating/cooling rate of 10 K min^{-1}.

Powder X-ray diffraction (PXRD) patterns were collected on a Thermo ARL X'TRA powder diffractometer (CuK_α radiation, $\lambda = 1.5418$ Å, Bragg–Brentano geometry, Peltier-cooled CCD detector) at T_R. PXRD data were collected at room temperature over the 5–65° 2θ range with 0.02° steps. The phase analysis was carried out using the Crystallographica Search-March program (Version 2.0.3.1) and JCPDS PDF-2 Data Base. The determination of the lattice parameters was performed using JANA2006. The Le Bail method [30] was applied to determine the lattice parameters, using the JANA2006 software [31]. The Rietveld analyses [32] were performed using the JANA2006 programme package [31]. Synchrotron PXRD data for $Ca_{9-x}Ba_xBi(VO_4)_7$ ($x = 0.25, 0.5$) were measured on a large Debye–Scherrer camera at the BL15XU beamline of SPring-8 [33,34]. The intensity data were collected from 1.978° to 60.180° in 2θ with a step of 0.003°; the incident beam was monochromatized at $\lambda = 0.65298$ Å. The samples were packed into Lindemann glass capillaries (with inner diameter of 0.1 mm), which were rotated during the measurement. The absorption coefficients were also measured.

The tests for optical second harmonic generation (SHG) were performed with a laser system in reflection geometry as described in *Ref.* [35].

For dielectric properties measurements we used samples in the form of pellets with flat surfaces from 20 to 60 mm^2 in area and 2–4 mm in height. The pellets were obtained by pressing at 1 kbar and sintering at 1193 K for 4 h. The densities of the resultant pellets were typically 90–95% of theoretical ones. Pt electrodes were put on flat surfaces of the pellets and then burned into at 1073 K (1 h). Electrical conductivity (σ), dielectric permittivity (ε') and dielectric loss tangent (tan δ) were calculated starting from complex impedance Z*. Dielectric investigations were produced on a Novocontrol Alpha-ANT impedance-analyzer with ZG4 interface in a ProboStat measuring cell using the double-contact method. The measurements were fulfilled in the frequency range of 1 Hz–3 MHz at stepwise heating-cooling cycle with the average rate of 0.7 K/min in between 600 and 1123 K.

3. Results and discussion

3.1. ICP-OES chemical analysis

The cation ratios of $Ca_{9-x}Ba_xBi(VO_4)_7$ ($x = 0, 0.25, 0.5$) were found to be Ca:Bi:V = 9.1(2): 1.03(3): 7.0(2) for $x = 0$; Ca:Ba:Bi:V = 8.6(3): 0.3(1): 1.00(3): 7.0(3): for $x = 0.25$ and Ca:Ba:Bi:V = 8.6(3): 0.5(1): 1.00(3): 7.0(3): for $x = 0.50$. Cation ratios found by ICP-OES analysis are close to the intended $Ca_{9-x}Ba_xBi(VO_4)_7$ ($x = 0, 0.25, 0.5$) compositions.

3.2. Preliminary characterization

Fig. 1 shows PXRD patterns of the $Ca_{9-x}Ba_xBi(VO_4)_7$ solid solutions with $0 \le x \le 1.0$. The samples with $0 \le x \le 0.7$ were single-phase, this fact shows that Bi^{3+} and Ba^{2+} cations were fully incorporated into the β-TCP-type host framework. However, the sample with $x = 0.8$ already contained additional reflections from impurities of $CaBaV_2O_7$ and $Bi_4V_2O_{10.5}$. Therefore, the solubility limit of Ba^{2+} in $Ca_{9-x}Ba_xBi(VO_4)_7$ is about 7.8%. Unit cell parameters were determined by the Le Bail method, and they are listed in Table 1. Substitution of Ba^{2+} ($r_{VIII}(Ba^{2+}) = 1.42$ Å [36]) for Ca^{2+} ($r_{VIII} = 1.12$ Å [36]) results in the increase of the lattice parameters (a and c) (Table 1).

3.3. DSC, SHG and dielectric measurements

Fig. 2 displays a fragment of typical heating/cooling DSC curves for $Ca_{9-x}Ba_xBi(VO_4)_7$ ($x = 0$, 0.25, 0.5) obtained at the heating/cooling rate of 10 K min^{-1}. The heating/cooling DSC curves indicate the presence of two peaks in the temperature range from 800 K to 1150 K for all x in the range $0 \le x \le 0.5$. The heating DSC curve for $Ca_9Bi(VO_4)_7$ exhibits two peaks: (1) $T_{min} = 1034$ K and (2) $T_{min} = 1101$ K (Fig. 2*a*). Along with the increase of Ba^{2+} content both thermal effects shift to lower temperatures (Fig. 2*b*). All peaks of heating and cooling DSC versus T curves for $Ca_{9-x}Ba_xBi(VO_4)_7$ ($x = 0$, 0.25, 0.5) detect endothermic and exothermic first-order phase transitions, respectively. The presence of two peaks on the cooling DSC curves exhibits that two first-order phase transitions (PT_1 and PT_2) are reversible and accompanied by an insignificant reconstruction of the structure.

The phase transitions in $Ca_{9-x}Ba_xBi(VO_4)_7$ ($x = 0$–0.7) are also detected by SHG measurements (Fig. 3). The substitution of Ca^{2+} by Ba^{2+} leads to increasing SHG signal intensity $I_{2\omega}/I_{2\omega}(SiO_2)$ in comparison with $Ca_9Bi(VO_4)_7$. Nonlinear optical activity of the $Ca_{9-x}Ba_xBi(VO_4)_7$ reaches their maximum response at $x = 0.5$ and the further increase of x leads to sharp decrease of response (Table 1). SHG response rapidly falls in the two-phase region ($0.7 < x \le 1.5$) due to decrease of the noncentrosymmetric phase

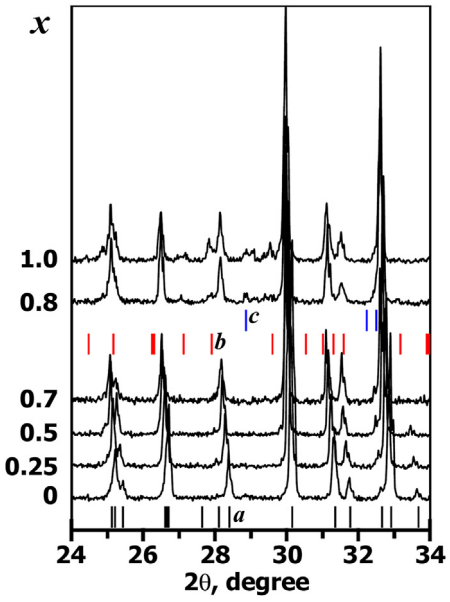

Fig. 1. Parts of XPRD pattern of $Ca_{9-x}Ba_xBi(VO_4)_7$ solid solutions. Bragg reflections for $Ca_9Bi(VO_4)_7$ (JCPDS, PDF-2, 46–404 (*a*)), $CaBaV_2O_7$ (JCPDS, PDF-2, 86–0117 (*b*)) and $Bi_4V_2O_{10.5}$ (JCPDS, PDF-2 89–4497 (*c*)) are shown.

Table 1
Lattice parameters, phase transition temperature (T_c) and value of the SHG ($I_{2\omega}/I_{2\omega}(SiO_2)$) response (±10%) for $Ca_{9-x}Ba_xBi(VO_4)_7$.

x	a, Å	c, Å	V, Å^3	T_c, ± 5 K	$I_{2\omega}/I_{2\omega}(SiO_2)/30 \pm 5$ μm
0	10.899(1)	38.120 (4)	3922.4(1)	1044	65
0.25	10.927 (3)	38.182 (3)	3948.7(1)	969	80
0.5	10.950(2)	38.240(2)	3970.1(1)	913	90
0.7	10.972(4)	38.267(4)	3989.6(2)	861	50
0.8[a]	10.9806(2)	38.2672(8)	3995.87(9)		
1.0[a]	10.990(6)	38.290(5)	4005.1(4)		30
1.25[a]	11.000(6)	38.332(6)	4016.6(4)		5
1.5[a]	11.008(7)	38.369(7)	4026.1(5)		6

[a] A two-phase sample.

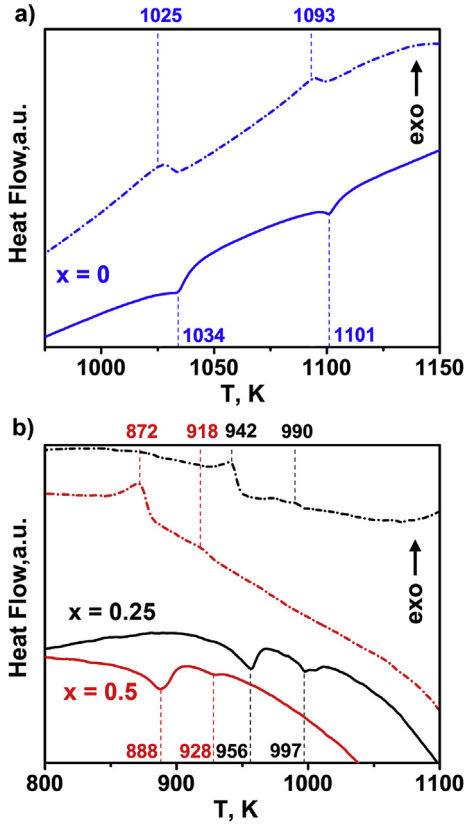

Fig. 2. Heating (solid lines)/cooling (dotted lines) DSC curves of $Ca_9Bi(VO_4)_7$ (a) and $Ca_{9-x}Ba_xBi(VO_4)_7$ ($x = 0.25$, 0.5) (*b*). Phase transition temperatures are marked by numbers.

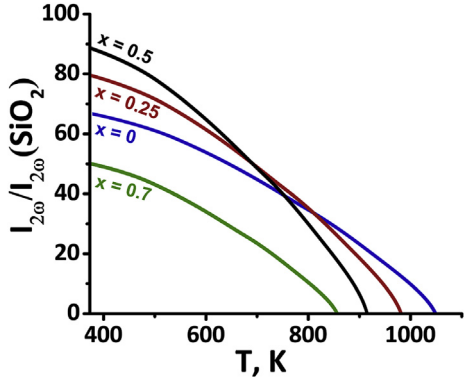

Fig. 3. Heating temperature dependence of SHG signals with a grain size of 30 ± 5 μm for $Ca_{9-x}Ba_xBi(VO_4)_7$.

content and decrease of the structural homogeneity of the crystallites. The SHG signal versus T curve during heating is shown in Fig. 3. The intensity of the SHG response gradually decreases with increasing temperature. Disappearance of SHG signal in $Ca_{9-x}Ba_xBi(VO_4)_7$ ($x = 0$–0.7) at temperatures above T_c corresponds to transition from polar noncentrosymmetrical phase into centrosymmetric one. The SHG signal is again restored during consequent cooling.

The temperature dependencies of dielectric permittivity (ε') and dielectric loss tangent ($\tan\delta$) for $Ca_{9-x}Ba_xBi(VO_4)_7$ are given in Fig. 4. Similar behavior of the dielectric constant and dielectric loss tangent is observed for all x in the range $0 \le x \le 0.7$. As shown in Fig. 4, all $\varepsilon'(T)$ curves demonstrate a characteristic maximum in the temperature range from 861 to 1044 K. The temperature position of this anomaly on the $\varepsilon'(T)$ curves does not depend on the frequency and is influenced only by the sample composition. Such anomaly is known to accompany ferroelectric as well as antiferroelectric phase transitions. The value of $\varepsilon'(T)$ maximum decreases with frequency increasing while its temperature does not change (Fig. 4) and coincides with temperature of disappearance of SHG response at heating.

This fact together with the presence of anomalies on the tan δ versus T curves in the temperature range from 800 to 1050 K (Fig. 4) allows to classify the phase transformation as a ferroelectric phase transition. Such tan δ (T) peak is characterized for ferroelectrics and related to the increasing mobility of domain walls while approaching to the temperature of the phase transition T_c. Besides the ferroelectric domains mobility, there is an Arrhenius-type mobility of electric charges, which may be assigned to the Ca^{2+} cation mobility often observed in the β-TCP-related compounds. The temperatures of maxima observed on the $\varepsilon'(T)$ curves for all x in the range $0 \le x \le 0.7$ are close to temperatures of first phase transition (PT_1) determined from heating DSC curves (Fig. 2) and temperatures (T_c) of SHG response disappearance (Fig. 3). Second phase transitions (PT_2) are observed as an anomaly on the $\varepsilon'(T)$ curves at high frequencies (Fig. 5). Fig. 5 displays a fragment of the $\varepsilon'(T)$ curves of $Ca_{9-x}Ba_xBi(VO_4)_7$ ($x = 0$, 0.25) at high frequencies. The temperature of the anomaly on the $\varepsilon'(T)$ curves at high frequencies is close to the temperature of second phase transition (PT_2) determined from heating DSC curves (Fig. 2).

3.4. Electric conductivity characterization

Ionic conductivity in β-TCP-type structure is provided by Ca^{2+} mobility [16,37]. It was previously shown that there are two [14] or three [38] possible pathways for Ca^{2+} ion conductivity: (I) … → *M*3 → *M*4 → *M*3' → *M*6 → *M*3"→ …, (II) … → *M*4 → *M*2 → *M*4′ and (III) … → *M*2 → $M4_3$ → *M*2' → *M*1 → *M*6 → *M*1'→→ *M*6 → *M*2"→ … While migrating along these pathways from one position (*M*) into another, each Ca^{2+} cation overcomes narrow sites ("bottlenecks"), formed by oxygen atoms. These narrow sites may be located on the common faces of calcium-centered or empty polyhedra or, in other case, between faces of adjacent calcium-centered polyhedra [37,38].

Cole-Cole diagrams of complex impedance Z^* for $Ca_{8.75}Ba_{0.25}Bi(VO_4)_7$ ($x = 0.25$) at different temperatures are shown in Fig. 6. Typical 2 semicircles in the impedance diagram are seen to be related to bulk and grain boundaries resistivity correspondingly. As it is often the case with solid solutions ceramics with non-uniform micro-structure, the semicircles are deformed and overlapped. The spectra are similar for those of all other single-phase compositions of $Ca_{9-x}Ba_xBi(VO_4)_7$ ceramics. An equivalent electric circuits (insert in Fig. 6) was applied to approximate experimentally obtained Cole-Cole diagrams. This procedure was fulfilled with the standard program Z-view (Scribner Associates).

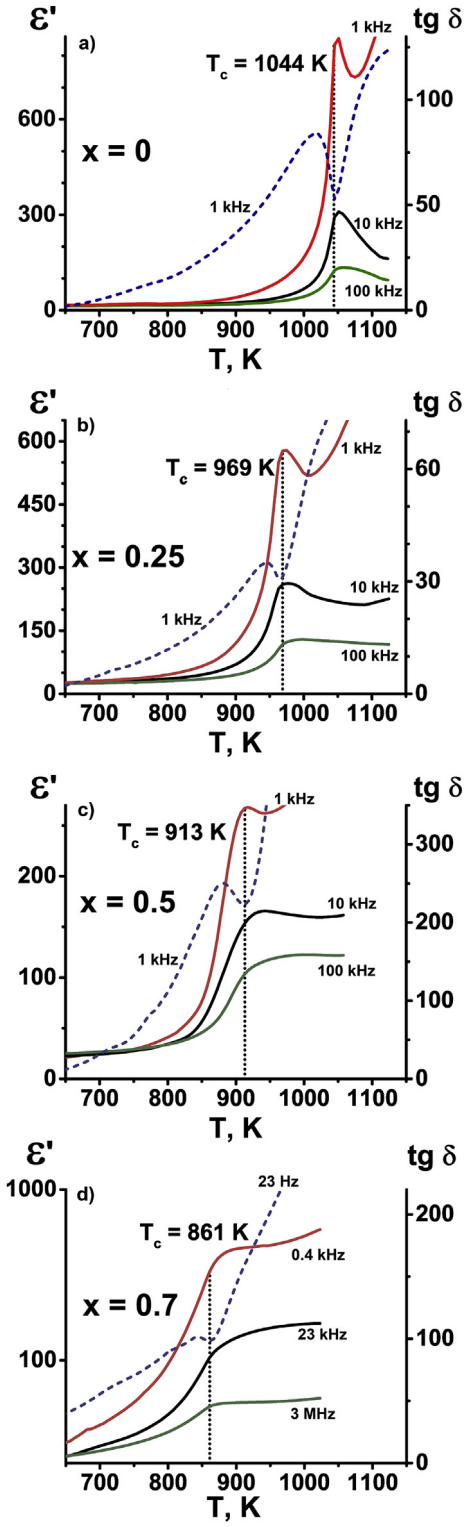

Fig. 4. Temperature dependencies of dielectric constant (ε' - solid lines) and dielectric loss tangent (tan δ - dotted lines) for $Ca_{9-x}Ba_xBi(VO_4)_7$, $x = 0$, 0.25, 0.5, 0.7.

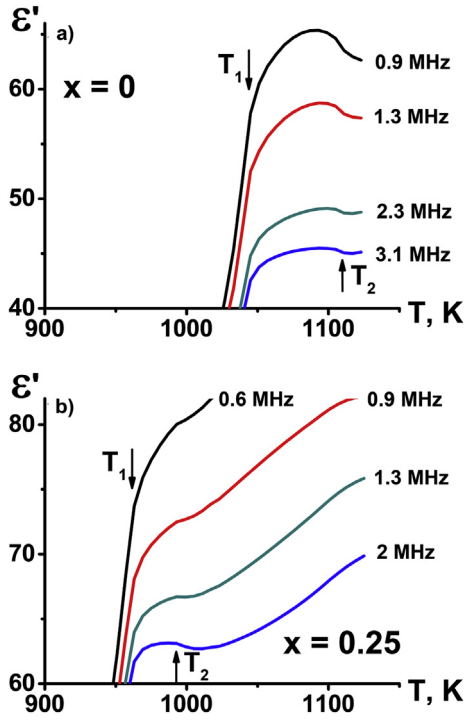

Fig. 5. Fragments of the ε'-T curves of $Ca_{9-x}Ba_xBi(VO_4)_7$ for $x = 0$ (a), 0.25 (b) at high frequencies and at high temperatures to emphasize anomalies at T_1 and T_2.

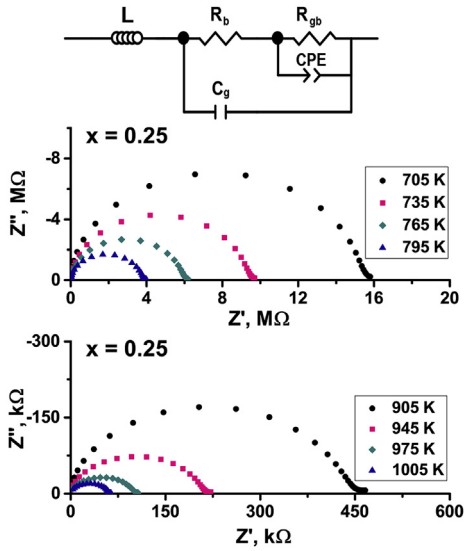

Fig. 6. Complex impedance plot of $Ca_{8.75}Ba_{0.25}Bi(VO_4)_7$ at selected temperatures. The upper part of the figure shows an equivalent scheme used for data fitting.

Temperature dependence of bulk conductivity (σ_b) for $Ca_{9-x}Ba_xBi(VO_4)_7$ is given in Fig. 7. Slope change on the temperature conductivity curves σ_b also proves restructuring at the given temperatures which is also confirmed by DSC data, dielectric measurements and temperature research of the SHG signals, in other words corresponds to the ferro-paraelectric phase transition. It is known from the published data that Ca^{2+} cations conductivity is realized in this class of compounds [16,37] by jump mechanism [14]. The values of high-temperature (HT) activation energy σ_b reveal that the activation energy (0.74–1.17 eV) is correlated with the composition of samples similar to the phase transition temperature. The low-temperature (LT) activation energy σ_b demonstrates the values from 0.66 to 1.03 eV.

3.5. *Crystal structure refinement of $Ca_{9-x}Ba_xBi(VO_4)_7$ ($x = 0.25$, 0.5)*

The structural data for $Ca_9Bi(VO_4)_7$ [5] were used as a starting

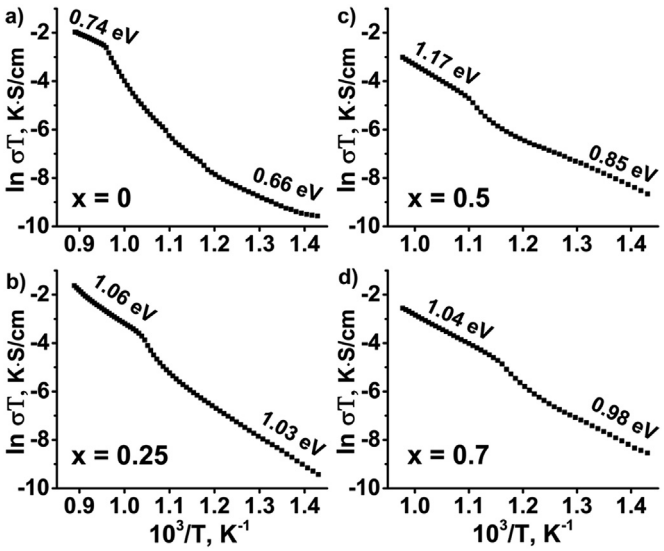

Fig. 7. Temperature dependence of bulk conductivity (σ_b) for $Ca_{9-x}Ba_xBi(VO_4)_7$, $x = 0$ (a), 0.25 (b), 0.5(c), 0.7(d) plotted as ln (σ_b*T) vs 1000/T.

model for the refinements of $Ca_{9-x}Ba_xBi(VO_4)_7$ ($x = 0.25$, 0.5) structures. At the first stage, the *f* curves for Ca^{2+} (*M*1-*M*5 sites) were used, and all parameters of the chosen model were refined. The analysis of the occupancies demonstrated (Table 2, $n_{f\text{-}Ca}$) that the Bi^{3+} and Ba^{2+} cations are distributed between the *M*1-*M*3 sites in $Ca_{9-x}Ba_xBi(VO_4)_7$. In accordance with the overview of cation distributions among the *M*1−*M*5 sites of the β-TCP structure, Bi^{3+} and Ba^{2+} cations substitute Ca^{2+} in *M*1-*M*3 positions [24]. The occupancy of the *M*4 position by Ca^{2+} is close to 0 and indicate that *M*4 positions are free. The occupancy of the *M*5 position by Ca^{2+} is close to 1 indicating that Ca^{2+} cations are located at the *M*5 site (Table 2).

At the second stage, the *f* curves for Bi^{2+} (*M*1-*M*3 sites) were used, and all parameters of the chosen model were refined. The distribution of the Bi^{3+} cations over the *M*1 and *M*3 positions in the $Ca_{9-x}Ba_xBi(VO_4)_7$ ($x = 0.25$, 0.5) structures was refined considering their multiplicities ($(M1 - M3) = nCa^{2+} + (1\text{-}n)Bi^{3+}$) but without stoichiometric constraints on the global Bi/Ca ratio. At the last stage, the distribution of the Ca^{2+}, Bi^{3+} and Ba^{2+} cations over the *M*1-*M*3 positions in the $Ca_{9-x}Ba_xBi(VO_4)_7$ ($x = 0.25$, 0.5) structures was refined considering their multiplicities ($M1 = mCa^{2+} + (1\text{-}m)Bi^{3+}$, $M2 = nCa^{2+} + (1\text{-}n)Bi^{3+}$, $M3 = xCa^{2+} + (0.333\text{-}n\text{-}m)Bi^{3+} + 0.0833Ba^{2+}$ for $x = 0.25$ and $M3 = xCa^{2+} + (0.333\text{-}n\text{-}m)Bi^{3+} + 0.1667Ba^{2+}$ for $x = 0.5$) with stoichiometric constraints on the global Ba/Bi/Ca ratio.

We also gave the same atomic displacement parameters to all O atoms. Final refinements were provided with independent Ba/Bi/Ca atomic coordinates as done in the refinement of the $Ca_{9.5-1.5x}Bi_xCd(VO_4)_7$ and $Ca_9Eu(PO_4)_7$ structures with independent Eu/Ca and Bi/Ca atomic coordinates [35,39].

The reliability factors R_{all} and R_p show a good agreement between the calculated and the experimental PXRD patterns. Fig. 8 displays a portion of the observed, calculated, and difference synchrotron PXRD patterns for $Ca_{9-x}Ba_xBi(VO_4)_7$ ($x = 0.25$, 0.5). Other numerical characteristics illustrating the quality of the structure refinements are presented in Table 2. The fractional atomic coordinates, isotropic atomic displacement parameters, cation occupancies and main relevant interatomic distances for $Ca_{9-x}Ba_xBi(VO_4)_7$ ($x = 0.25$, 0.5) are listed in Tables S1−S2 of the Supporting information.

$Ca_{9-x}Ba_xBi(VO_4)_7$ solid solutions with β-TCP-type structure (SG *R*3*c*) have been obtained by means of Ba^{2+} cations substitution for Ca^{2+} in $Ca_9Bi(VO_4)_7$ in the interval of $0 \le x \le 0.7$. In this interval the ferroelectric Curie point (T_c) dependence on Ba^{2+} content goes linearly down from $T_c = 1044$ K ($x = 0$) to 861 K ($x = 0.7$). Bi^{3+} and Ba^{2+} cations are completely incorporated into the β-TCP-type host framework up to $x = 0.7$. Further increase of Ba2+ content leads to the two-phase region and to the appearance of $CaBaV_2O_7$ and $Bi_4V_2O_{10.5}$ phases. Unit cell parameters of $Ca_{9-x}Ba_xBi(VO_4)_7$ ($0 \le x \le 0.7$) increase with increasing Ba^{2+} content.

Table 2
Crystallographic data for $Ca_{9-x}Ba_xBi(VO_4)_7$ (SP. GR. *R*3*c*, Z = 6, T = 293 K).

	$x = 0.25$	$x = 0.50$
Sample composition	$Ca_{8.75}Ba_{0.25}Bi(VO_4)_7$	$Ca_{8.50}Ba_{0.50}Bi(VO_4)_7$
Lattice parameters: *a*, Å	10.93309(1)	10.95945(1)
c, Å	38.20277(3)	38.26667(3)
Unit cell volume, Å^3	3954.680(6)	3980.419(6)
Calculated density, g/cm^3	3.52(1)	3.56(1)
Data Collection		
Diffractometer	BL15XU beamline of SPring-8	
Radiation/Wavelength (λ, Å)	Synchrotron/0.65298	
Used 2θ range (°)	4.054-39.638	4.054-51.455
Step scan (2θ)	0.003	0.003
Number of points	11860	15800
I_{max}	787815	898723
Refinement		
Refinement	Rietveld	
Background function	Legendre polynomials, 16 terms	
No. of reflections (All/observed)	1037/999	2183/2075
No. of refined parameters/refined atomic parameters	84/65	84/65
R, R_w (%) for Bragg reflections	5.94, 3.51	7.05, 3.79
R_P and R_{wP}; R_{exp} (%)	1.22, 2.08, 0.51	1.41, 2.45, 0.54
Goodness of fit (ChiQ)	4.11	4.58
Max./min. residual density	2.01/-1.47	3.37/-2.27
Selected crystal structure data		
$n_{f\text{-}Ca}M1$	1.195(5)	1.270(8)
$n_{f\text{-}Ca}M2$	1.308(6)	1.334(7)
$n_{f\text{-}Ca}M3$	1.693(9)	1.877(11)
$n_{f\text{-}Ca}M4$	~0	0.050(8)
$n_{f\text{-}Ca}M5$	1.046(7)	1.074(9)

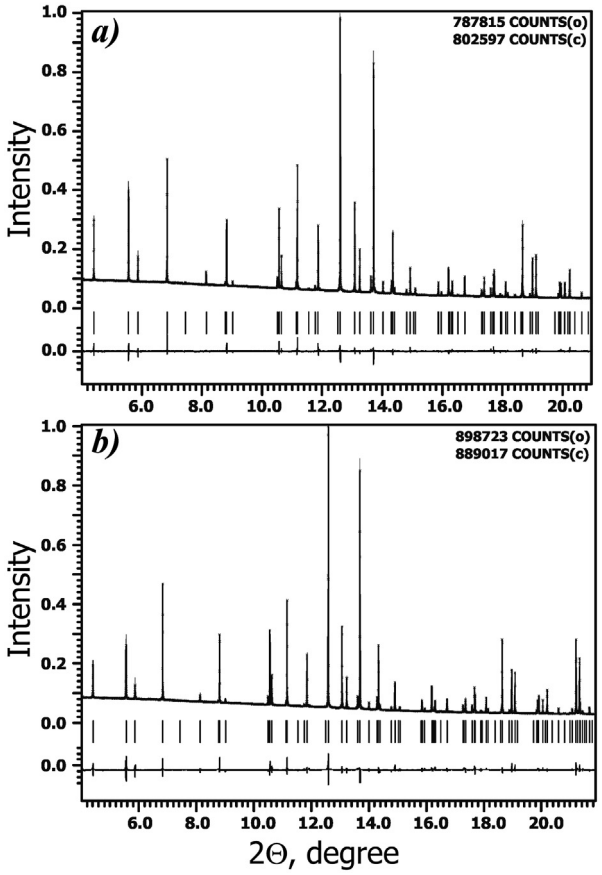

Fig. 8. Fragments of the observed, calculated and difference synchrotron PXRD patterns of $Ca_{8.75}Ba_{0.25}Bi(VO_4)_7$ (a) and $Ca_{8.50}Ba_{0.50}Bi(VO_4)_7$ (b). Tick marks denote the peak positions of possible Bragg reflections.

The β-TCP-related structures of $Ca_{9-x}Ba_xBi(VO_4)_7$ ($x = 0.25, 0.5$) solid solutions consist of isolated VO_4 tetrahedra that connect the MO_n polyhedra into a 3D framework *via* common vertices. According to crystal structure refinement small $M5O_6$ octahedra in $Ca_{9-x}Ba_xBi(VO_4)_7$ ($x = 0.25, 0.5$) are occupied by Ca^{2+} while Ca^{2+} and Bi^{3+} cations occupy $M1$-$M2$ positions β-TCP-type structure. Ba^{2+} cations together with Ca^{2+} and Bi^{3+} occupy largest $M3O_8$ polyhedra. $M1$–$M3$ (18-*fold*) and $M5$ (6-*fold*) positions are fully occupied while $M4$ (6-*fold*) and $M6$ (6-*fold*) sites are vacant.

On one side $Ca_{9-x}Ba_xBi(VO_4)_7$ structure can be built from two different layers along *c* axis, I and II, and two types of columns, *A* and *B* (Fig. 9*a*). Layer I consists of only *B* columns (Fig. 9*a*) while layer II has *A* and *B* columns (Fig. 9*b*). The *B* columns in the $Ca_3(VO_4)_2$ and $Ca_{9-x}Ba_xBi(VO_4)_7$ are similar and can be presented as [… –$M1O_8$–$M3O_8$–$M2O_8$–VO_4–VO_4– …]. The creation of vacancies in $M4$ site due to substitution of Ca^{2+} by Bi^{3+} leads to changing of *A* columns from […. –$V1O_4$–$Ca4O_{15}$–$Ca5O_6$–$M6O_{13}$(empty)– …] for $Ca_3(VO_4)_2$ to […. –$V1O_4$–$M4O_{15}$(empty)–$Ca5O_6$–$M6O_{13}$(empty)– …] for $Ca_{9-x}Ba_xBi(VO_4)_7$ phases.

On the other side the $Ca_{9-x}Ba_xBi(VO_4)_7$ structure is based on heteropolyhedral framework consisting of 12 layers of two types formed by $M3O_8$+$Ca5O_6$+$V2(V3)O_4$ polyhedra (L_1-layer) and $M1O_8$+$M2O_8$+$V1O_4$ polyhedra (L_2-layer) (Fig. 9*b*). Both layers alternate along [001] direction in the order … $|L_1L_2L_1L_2|$ …. L_1-layer contains $M3O_8$ and $Ca5O_6$-polyhedra which are linked by $V2O_4$ and $V3O_4$ tetrahedra (Fig. 10*a*). $M3O_8$ polyhedra linking *via* common edges form a $[M3_3O_{22}]$ cluster. Three $M3O_8$ polyhedra and three $V2O_4$ tetrahedra form a six-member ring with an unoccupied $M4$

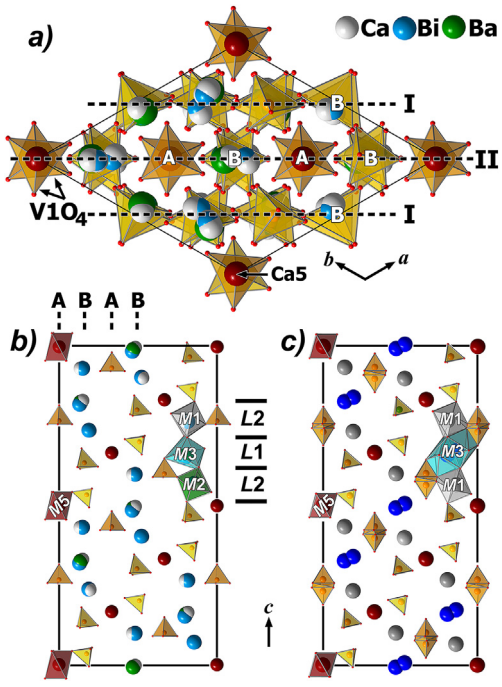

Fig. 9. *ab* projection of the $Ca_{8.50}Ba_{0.50}Bi(VO_4)_7$ structure (a). Layers II with the columns *A* and *B* (b, c) in the structure of the ferroelectric *R*3*c* $Ca_{8.50}Ba_{0.50}Bi(VO_4)_7$ phase (b) and in the structure of paraelectric $R\bar{3}c$ $Ca_9MgEu(PO_4)_7$ phase (c) are shown.

position in the center. L_2-layer contains $M1O_8$ and $M2O_8$ polyhedra which form a six-member ring. The center of each ring is occupied by $V1O_4$-tetrahedra (Fig. 10*b*).

Favorable conditions for second-order optical nonlinearity are created in $Ca_{9-x}Ba_xBi(VO_4)_7$ ($0 < x \leq 0.7$). Nonlinear optical activity of the $Ca_{9-x}Ba_xBi(VO_4)_7$ reaches their maximum response at $x = 0.5$ and further increase of *x* from 0.5 to 0.7 leads to sharp decrease of response. As shown in *Ref.* [35], the nonlinearity optical (NLO) coefficient should increase when the $M1$ and $M2$ positions in the ferroelectric *R*3*c* phase are occupied by different cations (different

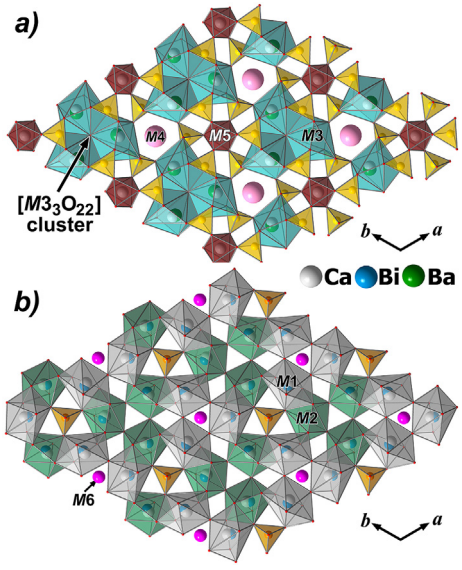

Fig. 10. Heteropolyhedral layers in the structure of $Ca_{8.50}Ba_{0.50}Bi(VO_4)_7$: L1-layer (a) and L2-layer (b). $M4$ and $M6$ positions are vacant.

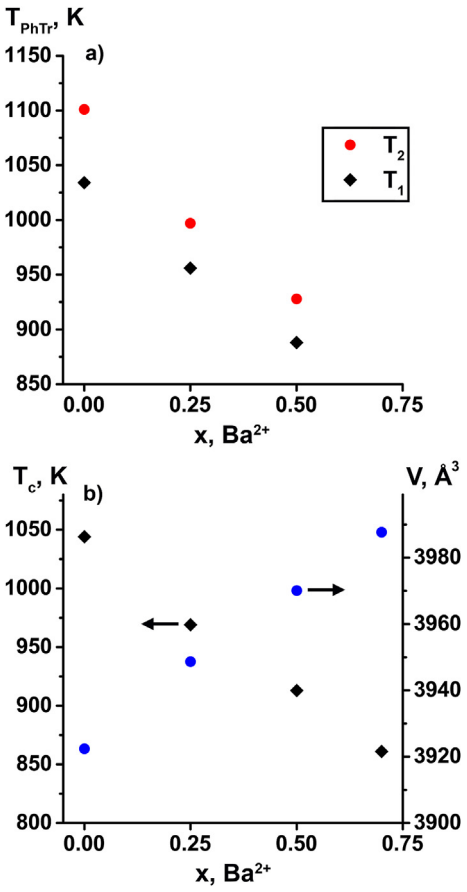

Fig. 11. Dependence of temperatures of anomalies at T_1 and T_2 (*a*), the lattice volume and phase transition temperature (T_c) (*b*) on the Ba^{2+} concentration in $Ca_{9-x}Ba_xBi(VO_4)_7$.

amounts of Ca^{2+} and Bi^{3+} cations), when they have a large difference between *M*1 – *M*3 and *M*2 – *M*3 distances. The splitting of *M*1 – *M*2 positions is insignificant and the Ca–Bi distances vary from 0.26(3) Å (Ca1–Bi1, $x = 0.25$) to 0.416(17) Å (Ca2–Bi2, $x = 0.25$). Ca3–Bi3 distances in $Ca_{9-x}Ba_xBi(VO_4)_7$ ($x = 0.25, 0.5$) solid solutions increase from 0.343(14) Å to 0.576(14) Å while Bi3–Ba3 distances decrease from 0.66(2) Å to 0.26(2) Å with increasing Ba^{2+} content from 0.25 to 0.5 (Table S2 of the Supporting information). In accordance with *Ref.* [35], (*M*1–(*M*3)–*M*2) dipoles make the main cation contribution to the overall NLO coefficient. Other ($M4_1$-$M4_2$) dipoles increasing the total NLO coefficient are absent in $Ca_{9-x}Ba_x$-$Bi(VO_4)_7$ structures [42]. Probably the amount of (*M*1–(*M*3)–*M*2) dipoles in $Ca_{9-x}Ba_xBi(VO_4)_7$ ($0 < x \leq 0.7$) increases with increasing Ba^{2+} content from 0.25 to 0.5 and decrease with changing *x* from 0.5 to 0.7.

DSC investigations of $Ca_{9-x}Ba_xBi(VO_4)$ ($x = 0$, 0.25, 0.5) revealed two reversible first-order phase transitions (PT_1 and PT_2) in the temperature range from 888 K to 928 K. Similar two phase transitions were earlier found for $Ca_9Yb(VO_4)_7$ [40] and $Ca_{9-x}Mg_xBi(VO_4)_7$ [41]. According to the SHG data the $Ca_{9-x}Ba_x$-$Bi(VO_4)_7$ structures are gradually changing up to the first phase transition temperature PT_1. Above this temperature the SHG signal vanishes and the β-TCP-type structure of $Ca_{9-x}Ba_xBi(VO_4)_7$ becomes centrosymmetric. Dielectric data give evidence of the ferroelectric-paraelectric nature of PT_1 transformation. Earlier we have found that ferroelectric-type phase transitions in β-TCP-type compounds are accompanied by symmetry change from noncentrosymmetric *R*3*c* to centosymmetric $R\bar{3}c$ [5,41–43].

Smaller enthalpy on DSC curves for PT_2 indicates another reconstruction of the crystal structure. Earlier the $R\bar{3}c \rightarrow R\bar{3}m$ antiferroelectric-type phase transition was found for Mg- and Zn-content β-TCP-related compounds [44,45]. $R\bar{3}m$ space group presents the highest symmetry possible in β-TCP-type compounds. This symmetry is the most probable for the highest-temperature phase in $Ca_{9-x}Ba_xBi(VO_4)_7$. Group-subgroup relations allow to restore the whole sequence of symmetry changes as $R3c \leftrightarrow R\bar{3}c \leftrightarrow R\bar{3}m$, occurring in this crystal at T_1 and T_2 correspondingly. Increase of Ba^{2+} content in $Ca_{9-x}Ba_xBi(VO_4)_7$ leads to lowering PT_1 and PT_2 phase transitions temperatures. It is possible that increasing the structure looseness due to the increase of cell volume with increasing Ba^{2+} content is the reason for this (Fig. 11).

The structure of the non-centrosymmetric (ferroelectric) *R*3*c* phase (Fig. 9*b*) is close to the structure of centrosymmetric $R\bar{3}c$ phase

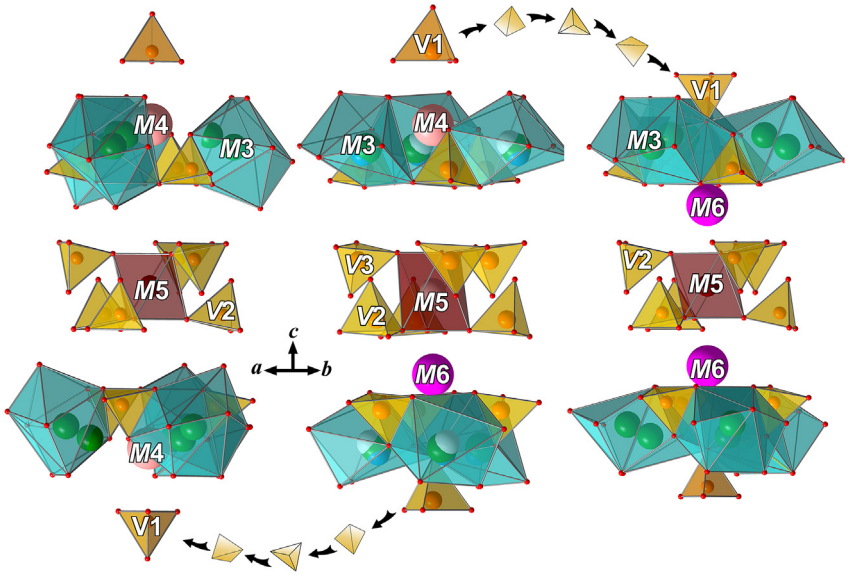

Fig. 12. The process of phase transition in $Ca_{9-x}Ba_xBi(VO_4)_7$ from the polar phase (*R*3*c*) into the centrosymmetric ($R\bar{3}c$) phase accompanied by changing in orientation of half of the $V1O_4$. *M*4 and *M*6 positions are vacant.

(Fig. 9*c*). The location of cations in *M*1-*M*3 positions in non-centrosymmetric (ferroelectric) *R*3*c* phase only slightly deviate from centrosymmetry. Therefore, small shifts of cations inside their polyhedra are required to transform cation moiety of crystal lattice into centrosymmetric. In $R\bar{3}c$ phase, the *M*3 site is located close to the center of symmetry (1/2, 0, 0) and the *M*1 and *M*2 sites, *M*4 and *M*6 sites are equivalent (connected by a center of symmetry). Anionic moiety becomes centrosymmetric as a result of turning-over of half of $V1O_4$ tetrahedra which are located on 3-*fold* axis near cation M4 position. Turning-over of these $V1O_4$ tetrahedra is an indispensable part of structural mechanism of ferroelectric phase transitions in β-TCP-type compounds. The *B* and *A* columns are transformed from [… −*M*1O_8−*M*3O_8−*M*2O_8−VO_4−VO_4− …] and […. −V1O_4−*M*4O_{15}(empty)−Ca5O_6−*M*6O_{13}(empty)− …] in the structure of *R*3*c* phase into [… −*M*1O_8−*M*3O_8−*M*1O_8−VO_4−VO_4− …] or […. −V1O_4−*M*4O_{15}(*M*6O_{13})−*M*5O_6−*M*4O_{15}(*M*6O_{13})− …] in paraelectric $R\bar{3}c$ phase (Fig. 12). It is also a key factor for understanding of dependences of ferroelectric T_c's in all the row of $Ca_{9-x}Ba_xBi(VO_4)_7$ regarding the cation size and the distribution over positions. Increase of Ba^{2+} content in $Ca_{9-x}Ba_xBi(VO_4)_7$ leads to increase of cell volume and decrease of steric hindrance for the flip of the $V1O_4$ tetrahedra.

4. Conclusion

$Ca_{9-x}Ba_xBi(VO_4)_7$ ($0 \le x \le 0.7$) solid solutions with the β-TCP-type structure were prepared by a solid-state method. $Ca_{9-x}Ba_xBi(VO_4)_7$ ($x = 0.25$, 0.5) structures were refined by the Rietveld method using powder synchrotron X-ray diffraction data and the distribution of Ca^{2+}, Ba^{2+} and Bi^{3+} cations among the sites of the β-TCP-type structure was found. SHG, DSC and dielectric spectroscopy proved existence of reversible ferroelectric phase transitions in $Ca_{9-x}Ba_xBi(VO_4)_7$ ($0 < x \le 0.7$) solid solutions in the range from 1044 K to 861 K. The substitution of Ca^{2+} by Ba^{2+} leads to increasing SHG signal intensity $I_{2\omega}/I_{2\omega}(SiO_2)$ in comparison with $Ca_9Bi(VO_4)_7$. SHG intensity of the $Ca_{9-x}Ba_xBi(VO_4)_7$ reaches their maximum response at $x = 0.5$ and further increase of x leads to sharp decrease of response. The temperature of the phase transition decreases in the course of replacement of Ca^{2+} for larger size Ba^{2+} cations. The phase transition from polar phase into centrosymmetric one is accompanied by complex reorganization of the β-TCP-type structure, which includes rotation of the $V1O_4$ tetrahedra on 3-*fold* axis (near *M*4 position), so that the *M*6 and *M*4 positions become equivalent. We showed that NLO properties of β-TCP-related compounds can be designed and increased by an order of magnitude through appropriate isovalent substitutions for Ca^{2+} cations.

Acknowledgements

This research was supported by Russian Science Foundation (Grant 16-13-10340). The synchrotron radiation experiments were performed at the SPring-8 with the approval of NIMS Synchrotron X-ray Station (Proposal Number: 2016B4504).

Appendix A. Supplementary data

Supplementary data to this article can be found online at https://doi.org/10.1016/j.jallcom.2019.03.365.

References

[1] B. Dickens, L.W. Schroeder, W.E. Brown, Crystallographic studies of role of Mg^{2+} as a stabilizing impurity in β-$Ca_3(PO_4)_2$. 1. Crystal-structure of pure β-$Ca_3(PO_4)_2$, J. Solid State Chem. 10 (1974) 232–248.
[2] R. Gopal, C. Calvo, Structure of $Ca_3(VO_4)_2$, Z. Kristallogr. 137 (1973) 67–85.
[3] C. Calvo, R. Gopal, Crystal-structure of whitlockite from Palermo quarry, Am. Mineral. 60 (1975) 120–133.
[4] I.A. Leonidov, L.L. Surat, O.N. Leonidova, R.F. Samigullina, System $Ca_3(VO_4)_2$-Na_3VO_4-$LaVO_4$, Russ. J. Inorg. Chem. 48 (2003) 1720–1724.
[5] B.I. Lazoryak, O.V. Baryshnikova, S.Y. Stefanovich, A.P. Malakho, V.A. Morozov, A.A. Belik, I.A. Leonidov, O.N. Leonidova, G. Van Tendeloo, Ferroelectric and ionic-conductive properties of nonlinear-optical vanadate $Ca_9Bi(VO_4)_7$, Chem. Mater. 15 (2003) 3003–3010.
[6] H. Ning, H. Yan, M.J. Reece, A high curie point ferroelectric ceramic $Ca_3(VO_4)_2$, Ferroelectrics 487 (2015) 94–100.
[7] S.Y. Stefanovich, A.A. Belik, M. Azuma, M. Takano, O.V. Baryshnikova, V.A. Morozov, B.I. Lazoryak, O.I. Lebedev, G. Van Tendeloo, Antiferroelectric phase transition in $Sr_9In(PO_4)_7$, Phys. Rev. B Condens. Matter 70 (2004) 172103.
[8] A.L. Mackay, D.P. Sinha, Piezo-electric activity of whitlockite β-$Ca_3(PO_4)_2$, J. Phys. Chem. 28 (1967) 1337–1338.
[9] M.S. Kim, S.M. Park, H.K. Kim, Optical properties of $Ca_{1.29}Bi_{0.14}VO_4$ crystal, J. Ind. Eng. Chem. 6 (2000) 144–148.
[10] D.A. Beskorovaynaya, D.V. Deyneko, O.V. Baryshnikova, S.Y. Stefanovich, B.I. Lazoryak, Optical non-linearity tuning in $Ca_{8-x}Pb_xMBi(VO_4)_7$ whitlockite-type systems, J. Alloys Compd. 674 (2016) 323–330.
[11] Z. Lin, G. Wang, L. Zhang, Growth of a new nonlinear optical crystal $YCa_9(VO_4)_7$, J. Cryst. Growth 304 (2007) 233–235.
[12] L. Huang, N. Zhuang, G. Zhang, J. Chen, C. Huang, B. Zhao, Y. Wei, X. Hu, M. Wei, Accurate measurement of refractive indices of $Ca_9La(VO_4)_7$ crystal, Opt. Mater. 31 (2008) 372–374.
[13] I.A. Leonidov, O.N. Leonidova, L.L. Surat, L.V. Kristallov, L.A. Perelyaeva, R.F. Samigullina, Phase of variable composition in the $Ca_3(VO_4)_2$-$NdVO_4$-Na_3VO_4, Russ. J. Inorg. Chem. 46 (2001) 268–273.
[14] I.A. Leonidov, A.A. Belik, O.N. Leonidova, B.I. Lazoryak, Structural aspects of calcium ion transport in $Ca_3(VO_4)_2$ and $Ca_{3-x}Nd_{2x/3}(VO_4)_2$ solid solutions, Russ. J. Inorg. Chem. 47 (2002) 305–312.
[15] D. Wei, Y. Huang, J.S. Kim, L. Shi, H.J. Seo, Electrical properties of $Ca_9ZnLi(PO_4)_7$ ceramics prepared by reactive pressureless sintering, J. Electron. Mater. 39 (2010) 441–446.
[16] I.A. Leonidov, O.N. Leonidova, L.L. Surat, R.F. Samigullina, $Ca_3(VO_4)_2$-$LaVO_4$ cation conductors, Russ. J. Inorg. Mater. 39 (2003) 616–620.
[17] W. Sun, Y. Jia, R. Pang, H. Li, T. Ma, D. Li, J. Fu, S. Zhang, L. Jiang, C. Li, $Sr_9Mg_{1.5}(PO_4)_7$:Eu^{2+}: a novel broadband orange-yellow-emitting phosphor for blue light-excited warm white LEDs, ACS Appl. Mater. Interfaces 7 (2015) 25219–25226.
[18] L. Li, X.G. Liu, H.M. Noh, J.H. Jeong, Chemical bond parameters and photoluminescence of a natural-white-light $Ca_9La(VO_4)_7$:Tm^{3+}, Eu^{3+} with one O^{2-}–V^{5+} charge transfer and dual f-f transition emission centers, J. Solid State Chem. 221 (2015) 95–101.
[19] M. Shang, S. Liang, H. Lian, J. Lin, Luminescence properties of $Ca_{19}Ce(PO_4)_{14}$:A (A = Eu^{3+}/Tb^{3+}/Mn^{2+}) phosphors with abundant colors: abnormal coexistence of Ce^{4+}/$^{3+}$–Eu^{3+} and energy transfer of Ce^{3+} → Tb^{3+}/Mn^{2+} and Tb^{3+}–Mn^{2+}, Inorg. Chem. 56 (2017) 6131–6140.
[20] M. Chen, Z. Xia, M.S. Molokeev, C.C. Lin, C. Su, Y.C. Chuang, Q. Liu, Probing Eu^{2+} luminescence from different crystallographic sites in $Ca_{10}M(PO_4)_7$:Eu^{2+} (M = Li, Na, and K) with β-$Ca_3(PO_4)_2$-type structure, Chem. Mater. 29 (2017) 7563–7570.
[21] S. Sun, Z. Lin, L. Zhang, Y. Huang, G. Wang, Growth and spectral properties of a new nonlinear laser crystal of Nd^{3+}:$Ca_9Y_{0.5}La_{0.5}(VO_4)_7$, J. Alloys Compd. 551 (2013) 229–232.
[22] P.A. Loiko, A.S. Yasukevich, A.E. Gulevich, M.P. Demesh, M.B. Kosmyna, B.P. Nazarenko, V.M. Puzikov, A.N. Shekhovtsov, A.A. Kornienko, E.B. Dunina, N.V. Kuleshov, K.V. Yumashev, Growth, spectroscopic and thermal properties of Nd-doped disordered $Ca_9(La/Y)(VO_4)_7$ and $Ca_{10}(Li/K)(VO_4)_7$ crystals, J. Lumin. 137 (2013) 252–258.
[23] B.I. Lazoryak, Design of inorganic compounds with tetrahedral anions, Russ. Chem. Rev. 65 (1996) 287–305.
[24] D.V. Deyneko, V.A. Morozov, J. Hadermann, A.E. Savon, D.A. Spassky, S.Y. Stefanovich, A.A. Belik, B.I. Lazoryak, A novel red $Ca_{8.5}Pb_{0.5}Eu(PO_4)_7$ phosphor for light emitting diodes application, J. Alloys Compd. 647 (2015) 965–972.
[25] D. Phanon, Y. Suffren, M.B. Taouti, D. Benbertal, A. Brenier, I. Gautier-Luneau, Optical properties of Nd^{3+} and Yb^{3+}-doped $AgM(IO_3)_4$ metal iodates: transparent host matrices for mid-IR lasers and nonlinear materials, J. Mater. Chem. C. 2 (2014) 2715–2723.
[26] K.B. Chang, D.H. Hubbard, M. Zeller, J. Schrier, A.J. Norquist, The role of stereoactive lone pair in template vanadium tellurite charge density matching, Inorg. Chem. 49 (2010) 5167–5172.
[27] K.M. Ok, P.S. Halasyamani, New metal iodates: syntheses, structures, and characterizations of noncentrosymmetric $La(IO_3)_3$ and $NaYI_4O_{12}$ and Centrosymmetric $Cs_2I_4O_{11}$ and $Rb_2I_6O_{15}(OH)_2H_2O$, Inorg. Chem. 44 (2005) 9353–9359.
[28] Q. Wu, H.M. Liu, F.C. Jiang, L. Kang, L. Yang, Z.S. Lin, Z.G. Hu, X.G. Chen, X.G. Meng, J.G. Qin, $RbIO_3$ and $RbIO_2F_2$: Two promising nonlinear optical materials in mid-IR region and influence of partially replacing oxygen with fluorine for improving laser damage threshold, Chem. Mater. 28 (2016) 1413–1418.
[29] S.W. Bae, J. Yoo, S. Lee, K.Y. Choi, K.M. Ok, Synthesis and characterization of three new layered vanadium tellurites, $MVTe_2O_8$ (M = Al, Ga and Mn): three-dimensional (3-D) antiferromagnetic behavior of $MnVTe_2O_8$ with a zigzag s =

2 spin chain, Inorg. Chem. 55 (2016) 1347–1353.
[30] A. Le Bail, H. Duroy, J.L. Fourquet, Ab-initio structure determination of $LiSbWO_6$ by X-ray powder diffraction, Mater. Res. Bull. 23 (1988) 447–452.
[31] V. Petricek, M. Dusek, L. Palatinus, Crystallographic computing system JANA2006: general features, Z. Kristallogr. 229 (2014) 345–352.
[32] H.M. Rietveld, A Profile refinement method for nuclear and magnetic structures, J. Appl. Crystallogr. 2 (1969) 65–71.
[33] M. Tanaka, Y. Katsuya, A. Yamamoto, A new large radius imaging plate camera for high-resolution and high-throughput synchrotron X-Ray powder diffraction by multiexposure method, Rev. Sci. Instrum. 79 (2008), 075106.
[34] M. Tanaka, Y. Katsuya, Y. Matsushita, O. Sakata, Development of a synchrotron powder diffractometer with a one-dimensional X-Ray detector for analysis of advanced materials, J. Ceram. Soc. Jpn. 121 (2013) 287–290.
[35] N.G. Dorbakov, O.V. Baryshnikova, V.A. Morozov, A.A. Belik, Y. Katsuya, M. Tanaka, S.Y. Stefanovich, B.I. Lazoryak, Tuning of nonlinear optic and ferroelectric properties via the cationic composition of $Ca_{9.5-1.5x}Bi_xCd(VO_4)_7$ solid solutions, Mater. Des. 116 (2017) 515–523.
[36] R.D. Shannon, Revised effective ionic-radii and systematic studies of interatomic distances in halides and chalcogenides, Acta Crystallogr. A 32 (1976) 751–767.
[37] I.A. Leonidov, M.Y. Khodos, A.A. Fotiev, A.S. Zhukovskaya, Effect of vacancies on Ca^{45} diffusion in the solid solutions $Ca_{3(1-x)}Eu_{2x}(VO_4)_2$, Russ. J. Inorg. Mater. 24 (1988) 280–281.
[38] S.Y. Stefanovich, D.A. Petrova, V.A. Morozov, E.A. Fortalnova, D.A. Belov, D.V. Deyneko, O.V. Barishnikova, A.A. Belik, B.I. Lazoryak, Enhanced nonlinear optical activity and Ca^{2+}-conductivity in $Ca_{10.5-x}Pb_x(VO_4)_7$ ferroelectrics, J. Alloys Compd. 735 (2018) 1826–1837.
[39] R.A. Benhamou, A. Bessiere, G. Wallez, B. Viana, M. Elaatmani, M. Daoud, A. Zegzouti, New insight in the structure – luminescence relationships of $Ca_9Eu(PO_4)_7$, J. Solid State Chem. 182 (2009) 2319–2325.
[40] B.I. Lazoryak, S.M. Aksenov, S.Y. Stefanovich, N.G. Dorbakov, D.A. Belov, O.V. Barishnikova, V.A. Morozov, M.S. Manylov, Z. Lin, Ferroelectric crystal $Ca_9Yb(VO_4)_7$ in the series of $Ca_9R(VO_4)_7$ non-linear optical materials (R = REE, Bi, Y), J. Mater. Chem. C. 5 (2017) 2301–2310.
[41] N.G. Dorbakov, V.V. Grebenev, V.V. Titkov, E.S. Zhukovskaya, S.Y. Stefanovich, O.V. Barishnikova, D.V. Deyneko, V.A. Morozov, A.A. Belik, Y. Katsuya, M. Tanaka, B.I. Lazoryak, Influence of magnesium on ferroelectricity in $Ca_{9-x}Mg_xBi(VO_4)_7$ ceramics, J. Am. Ceram. Soc. 101 (2018) 4011–4022.
[42] V.A. Morozov, A.A. Belik, S.Y. Stefanovich, V.V. Grebenev, O.I. Lebedev, G. Van Tendeloo, B.I. Lazoryak, High-temperature phase transition in the whitlockite-type phosphate $Ca_9In(PO_4)_7$, J. Solid State Chem. 165 (2002) 278–288.
[43] B.I. Lazoryak, V.A. Morozov, A.A. Belik, S.Y. Stefanovich, V.V. Grebenev, I.A. Leonidov, E.B. Mitberg, S.A. Davydov, O.I. Lebedev, G. Van Tendeloo, Ferroelectric phase transition in whitlockite-type phosphate $Ca_9Fe(PO_4)_7$ and crystal structure of paraelectric, ionic-conductive phase at 923 K, Solid State Sci. 6 (2004) 185–195.
[44] A.A. Belik, V.A. Morozov, D.V. Deyneko, A.E. Savon, O.V. Barishnikova, E.S. Zhukovskaya, N.G. Dorbakov, Y. Katsuya, M. Tanaka, S.Y. Stefanovich, J. Hadermann, B.I. Lazoryak, Antiferroelectric properties and site occupations of R^{3+} cations in $Ca_8MgR(PO_4)_7$ luminescent host materials, J. Alloys Compd. 699 (2017) 928–937.
[45] B.I. Lazoryak, E.S. Zhukovskaya, O.V. Barishnikova, A.A. Belik, O.N. Leonidova, D.V. Deyneko, A.E. Savon, N.G. Dorbakov, V.A. Morozov, Luminescence, structure and high-temperature phase transition of new antiferroelectric $Ca_8ZnEu(PO_4)_7$, Mater. Res. Bull. 104 (2018) 20–26.